The Astrophysical Journal, 774:39 (14pp), 2013 September 1 doi:10.1088/0004-637X/774/1/39


# ALMA OBSERVATIONS OF THE HH 46/47 MOLECULAR OUTFLOW

Héctor G. Arce[1], Diego Mardones[2], Stuartt A. Corder[3], Guido Garay[2], Alberto Noriega-Crespo[4], and Alejandro C. Raga[5]
[1] Department of Astronomy, Yale University, P.O. Box 208101, New Haven, CT 06520-8101, USA
[2] Departamento de Astronomía, Universidad de Chile, Casilla 36-D, Santiago, Chile
[3] Joint ALMA Observatory, Av. Alonso de Córdova 3107, Vitacura, Santiago, Chile
[4] Infrared Processing and Analysis Center, California Institute of Technology, Pasadena, CA 91125, USA
[5] Instituto de Ciencias Nucleares, UNAM, Ap. 70-543, 04510 D.F., Mexico
*Received 2013 March 31; accepted 2013 July 8; published 2013 August 14*

## ABSTRACT

The morphology, kinematics, and entrainment mechanism of the HH 46/47 molecular outflow were studied using new ALMA Cycle 0 observations. Results show that the blue and red lobes are strikingly different. We argue that these differences are partly due to contrasting ambient densities that result in different wind components having a distinct effect on the entrained gas in each lobe. A 29 point mosaic, covering the two lobes at an angular resolution of about 3″, detected outflow emission at much higher velocities than previous observations, resulting in significantly higher estimates of the outflow momentum and kinetic energy than previous studies of this source, using the CO(1–0) line. The morphology and the kinematics of the gas in the blue lobe are consistent with models of outflow entrainment by a wide-angle wind, and a simple model describes the observed structures in the position–velocity diagram and the velocity-integrated intensity maps. The red lobe exhibits a more complex structure, and there is evidence that this lobe is entrained by a wide-angle wind and a collimated episodic wind. Three major clumps along the outflow axis show velocity distribution consistent with prompt entrainment by different bow shocks formed by periodic mass ejection episodes which take place every few hundred years. Position–velocity cuts perpendicular to the outflow cavity show gradients where the velocity increases toward the outflow axis, inconsistent with outflow rotation. Additionally, we find evidence for the existence of a small outflow driven by a binary companion.

*Key words:* Herbig-Haro objects – ISM: clouds – ISM: individual objects (HH 46, HH 47) – ISM: jets and outflows – stars: formation

*Online-only material:* color figures

## 1. INTRODUCTION

As stars form inside molecular clouds, they eject mass in energetic bipolar outflows. The resulting bipolar wind from a young stellar object (YSO) may reveal itself through Herbig–Haro (HH) objects observed in the optical, $H_2$ emission knots in the infrared (IR), and molecular (CO) outflows observed at millimeter (mm) wavelengths. HH objects delineate highly collimated jets and their (internal or leading) bow shocks. The $H_2$ IR emission also arises from recently shocked gas and in many cases it traces the bow-shock wings that extend toward the driving source. CO outflows map the ambient gas that has been swept up well after it has been entrained by the protostellar wind and has cooled. Hence, these different manifestations provide complementary views: while HH objects and $H_2$ emission provide a "snapshot" of the current shock interaction, the CO outflow trace the protostar's mass loss history (e.g., Richer et al. 2000).

Protostellar winds inject energy and momentum into the surroundings, thereby perturbing the star formation environment. Outflows may be responsible for the clearing of material from the core (Arce & Sargent 2006), a process that could result in the termination of the infall phase (e.g., Velusamy & Langer 1998), affect the star formation efficiency in the cloud (e.g., Matzner & McKee 2000; Nakamura & Li 2007; Machida & Hosokawa 2013), and determine the mass of stars (Myers 2008). In addition, outflows can affect the kinematics, density, and chemistry of a substantial volume of their parent clouds, and thus can be important to the turbulent dynamics and energetics of their host cores. How exactly protostellar winds entrain and disperse the surrounding gas and feed their parent clouds turbulence remains a mystery. High angular (and velocity) resolution, multi-wavelength observations of outflows are needed to probe all different outflow manifestations in order to compare them with hydrodynamic numerical simulations and shock models to obtain a complete picture of protostellar winds, the entrainment process, and their impact on their surroundings.

Here we present Atacama Large Millimeter/sub-millimeter Array (ALMA) observations of the HH 46/47 molecular outflow. The high-resolution data were obtained with the aim of studying the entrainment process, the underlying protostellar wind, and the properties of the molecular outflow. The observed outflow is driven by HH 47 IRS (a.k.a. HH 46 IRS 1, IRAS 08242-5050), a low-mass Class I YSO with a total luminosity of about 12 $L_\odot$ in the Bok globule ESO 216-6A, located on the outskirts of the Gum Nebula at a distance of 450 pc (Schwartz 1977; Reipurth et al. 2000; Noriega-Crespo et al. 2004). The source lies very close to the edge of the Bok globule, which explains why the blue (northern) lobe of the HH 46/47 bipolar flow is clearly seen at optical wavelengths outside the globule, while within ∼2′ of the source the red lobe (which mostly lies inside the globule) is best seen in IR images. *Hubble Space Telescope* (*HST*) observations indicate that HH 47 IRS is actually a binary system, where the two components of the system are observed to be separated by only 0.″26 or about 120 AU (Reipurth et al. 2000). Wide-field, narrowband H$\alpha$ and [S II] optical images of the region by Stanke et al. (1999) reveal two groups of HH objects at distances, from the position of HH 47 IRS, of about 1.3 pc to the northeast (in the blue lobe) and

southwest (in the red lobe), outside the parent globule. These results showed that the well-known HH 46/47 flow (extending 0.57 pc from HH 47D in the northeast to HH 47C to the southwest) is, in fact, the innermost part of a giant HH flow that extends 2.6 pc on the plane of the sky.

Many of the properties of the HH 46/47 flow have been determined through extensive optical and IR observations. The combination of optical spectral data and proper motion studies of the HH knots (using ground-based telescopes) allowed an estimate of the flow's inclination to the plane of the sky ($\sim$30°) and an average jet velocity of 300 km s$^{-1}$ (Reipurth 1989; Reipurth & Heathcote 1991; Eislöeffel & Mundt 1994; Micono et al. 1998). More recently, proper motion studies (using *HST*) of the blue lobe optical HH knots, in combination with the results from spectroscopic Fabry–Perót observations (Morse et al. 1994), allowed Hartigan et al. (2005) to estimate an average orientation angle, with respect to the plane of the sky, of about 37°. Infrared images show how shocked $H_2$ emission in the southwestern (redshifted) lobe traces the walls of a 36″ (0.08 pc) wide cavity that extends $\sim$2′ (0.26 pc) to the position of HH 47C (Eislöffel et al. 1994; Noriega-Crespo et al. 2004).

The HH 46/47 molecular outflow has only been fully mapped at low resolution (with beams larger than 24″) by several authors, using the two lowest rotational transitions of CO (Chernin & Masson 1991; Olberg et al. 1992; van Kempen et al. 2009). APEX observations of higher CO transitions (up to 7–6) of a smaller area (80″ × 80″) surrounding the source show the molecular outflow gas reaches temperatures as high as 100 K (van Kempen et al. 2009). Moreover, recent *Herschel* PACS observations of a region within 30″ from the source reveal the existence of hot CO and $H_2O$ (thought to be partly produced by non-dissociative C-shocks) and OH and [O I] emission from dissociative J-shocks where the protostellar wind interacts with the surrounding dense core (van Kempen et al. 2010; Wampfler et al. 2010).

Even though the extensive multi-wavelength studies of this source have helped understand the physics of protostellar jets, the lack of high-resolution molecular outflow observations (until now) has hampered our ability to obtain a complete picture of the outflow phenomenon in HH 46/47, the entrainment process, and the protostellar wind's impact on the cloud. Here we present the first interferometric, high-resolution (beam $\sim$3″) observations of the HH 46/47 molecular (CO) outflow and compare the morphology and kinematics to existing (simple) models of outflow entrainment. In a future paper, we will use hydrodynamical simulations to model the outflow and aim to provide more stringent constraints on the launching and entrainment mechanisms in this flow.

## 2. OBSERVATIONS

The observations were carried out using ALMA from 2011 December 28 to 2012 January 25, during the Early Science Cycle 0 phase. The Band 3 data were obtained over 11 scheduling blocks, with 16–18 antennas in the (Cycle 0) compact configuration, consisting of projected baselines in the range of 12–277 m. The correlator was configured to observe three windows with the highest spectral resolution ($\delta\nu$ = 30.5 kHz), with a bandwidth of 58.6 MHz and centered at 115.27 GHz, the frequency of the CO (1–0) transition, and at 100.88 and 100.07 GHz. We only detected line emission in the 115.27 GHz window, which has a velocity resolution of 0.08 km s$^{-1}$. No line was detected in the other two windows, and were therefore used to map the continuum emission. We mapped our sources using a rectangular 29-point mosaic, with contiguous pointings separated by 24.″5, oriented at a position angle (P.A.) of about 58°, designed to cover the length of the HH 46/47 outflow from HH 47A, in the northeast, to HH 46C, in the southwest, and the width of the red outflow lobe seen in IR images (see, e.g., Noriega-Crespo et al. 2004). The mosaic had three rows, the two outer rows consisted of 10 pointings and the central row had 9, resulting in a map of about 1.′2 × 4.′2, centered on 08$^h$25$^m$41.$^s$5, −51°00′47″ (J2000).

The nearby quasar J0845−5458 was used for phase and gain calibration. Flux calibration was carried out using observations of Mars, and J0538−440 and 3c279 were used as bandpass calibrators. The visibility data were edited, calibrated, and imaged (using the CLEAN algorithm) in CASA, using 0.″5 cells and 1024 cells in each spacial dimension. For the spectral data we defined a different clean region for each channel, encircling the area with the brightest emission. The resulting synthesized beam for the $^{12}$CO(1–0) data cube is 3.″2 × 2.″4, with a P.A. = 16.°5, and the (1$\sigma$) rms is 25 mJy beam$^{-1}$ in a (spectroscopically smoothed) map with a velocity resolution of 0.5 km s$^{-1}$. The continuum was obtained by averaging the emission over all channels in the two windows close to 100 GHz with no detected line emission, resulting in a bandwidth of 117.2 MHz. The synthesized beam and rms for the continuum map are 3.″1 × 2.″2 (P.A. = 15°) and 0.33 mJy beam$^{-1}$.

## 3. RESULTS

### 3.1. Continuum Source

We detected continuum thermal dust emission at 100 GHz near the position of the protostar, with a peak intensity of 8.1 mJy beam$^{-1}$. A Gaussian fit puts the continuum peak at 8$^h$25$^m$43.$^s$8, −51°00′36″ (J2000.0), which we adopt as the position of HH 47 IRS, and it is consistent with that given by Reipurth et al. (2000). The continuum emission is barely resolved, and it is slightly extended toward the southwest (see Figure 1). The total flux density is 14 mJy, and we follow Schnee et al. (2010) and Dunham et al. (2012) to estimate the mass of the envelope using the dust continuum emission, assuming a dust temperature ($T_d$) of 30 K and gas-to-dust ratio of 100. We estimate the dust opacity ($\kappa$) at 3 mm to be 0.9 cm$^2$ g$^{-1}$, by extrapolating the value of $\kappa$ at 1.3 mm obtained by Ossenkopf & Henning (1994) for dust with a thin ice mantle after 10$^5$ yr of coagulation at a gas density of 10$^6$ cm$^{-3}$, and assuming an emissivity spectral index ($\beta$) of 1. Using the above assumptions, we obtain a total (gas and dust) mass associated with the continuum emission of 0.4 $M_\odot$. This estimate depends mostly on the assumed dust temperature, opacity, and emissivity index. Single-dish observations of the dust continuum of HH 47 by van Kempen et al. (2009) and observations of other Class 0 and Class I sources (e.g., Arce & Sargent 2006) indicate that $T_d$ in the range of 20–40 K is a reasonable assumption. The dust opacity at 3 mm can vary depending on the adopted dust model and the assumed $\beta$ (which may range from about 0.3 to 1.5 for Class 0 and Class I sources, e.g., Arce & Sargent 2006). Reasonable variations of these quantities lead to possible variations in the mass estimate by a factor of two to three.

The angular resolution of our continuum is not enough to resolve different peaks associated with the two different binary components of the system. The observed continuum emission most probably traces the envelope that surrounds the binary system, and observations with an order of magnitude

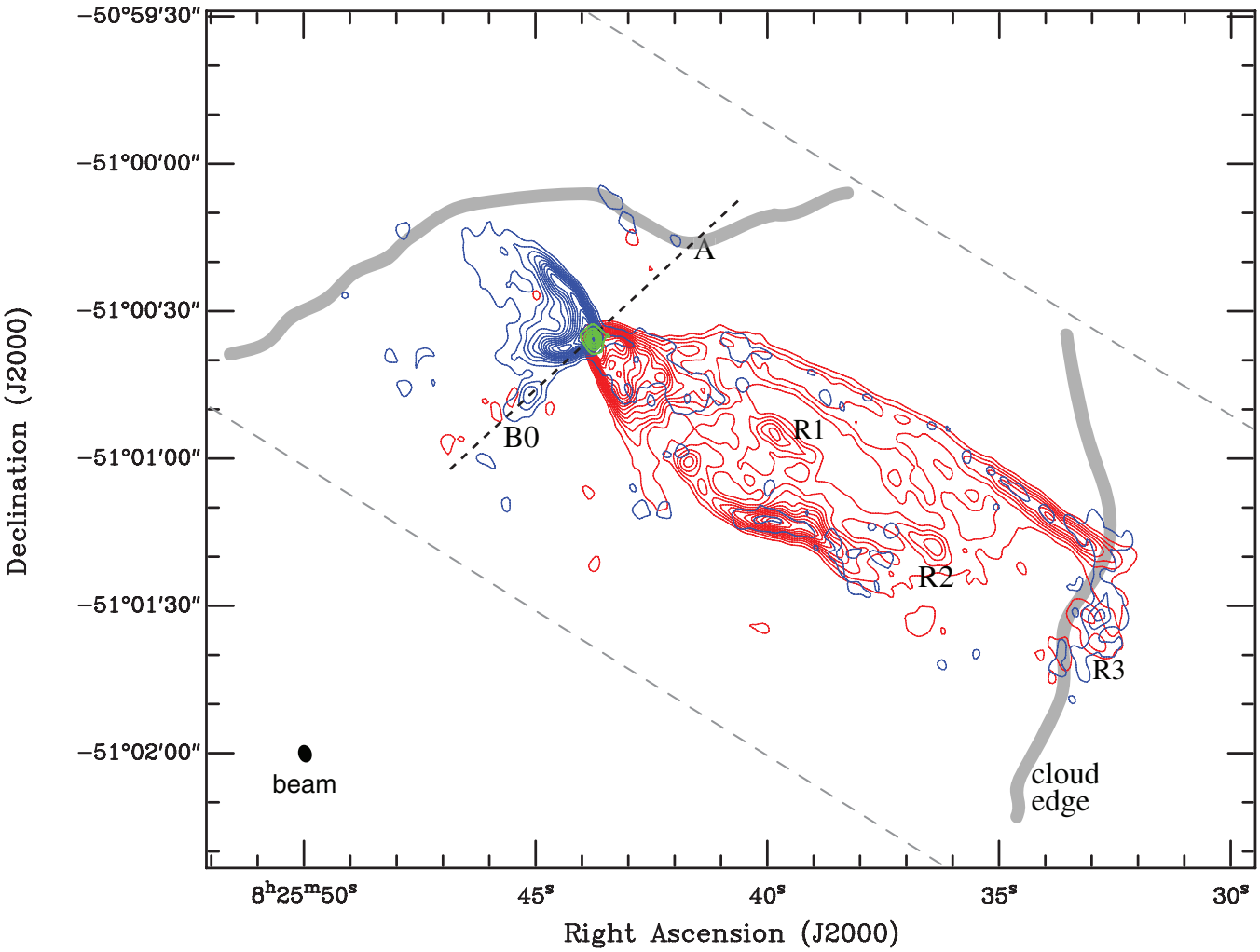


**Figure 1.** Integrated intensity map of the HH 46/47 CO(1–0) outflow. Blue (red) contours represent the blueshifted (redshifted) lobe. The blue lobe is integrated over $-6.8$ km s$^{-1}$ $< v_{\rm out} < -1.3$ km s$^{-1}$. The lowest contour and subsequent contour steps are 0.2 and 0.25 Jy beam$^{-1}$ km s$^{-1}$, respectively. The red lobe is integrated over 1.3 km s$^{-1}$ $< v_{\rm out} <$ 6.7 km s$^{-1}$. The lowest contour and subsequent contour steps are 0.25 and 0.3 Jy beam$^{-1}$ km s$^{-1}$, respectively. Green contours show the 3 mm continuum emission surrounding HH 47 IRS. The lowest contour and subsequent contour steps are 1.3 and 1 mJy beam$^{-1}$, respectively. The thick gray line delineates the edge of the globule as traced by our CO data close to the cloud velocity (see Figure 3). The synthesized beam of the CO map is shown on the lower left corner of the figure. Gray diagonal parallel dashed lines show the edges of our map. The position of redshifted outflow clumps R1, R2, and R3 is shown, as well as that of the blueshifted clump B0 and clump A. The dark dashed line passing through B0, HH 47 IRS, and A indicates the position of the $p$–$v$ cut shown in Figure 11. (A color version of this figure is available in the online journal.)

higher angular resolution are needed to investigate whether each component has its own separate circumstellar envelope.

### 3.2. Line Data and the Molecular Outflow

Integrated intensity maps of the CO(1–0) blueshifted and redshifted emission from the HH 46/47 molecular outflow are displayed in Figure 1. The most striking aspect of this outflow is the clear difference in size and morphology between the two different lobes; the red (southwestern) lobe extends approximately 2′ from the source, while the blue (northeastern) lobe only extends up to about 30″ from the powering YSO. This asymmetry had been noted in earlier, lower angular resolution observations of the CO outflow and it is generally assumed that it is due to the fact that the HH 47 IRS is close to the edge of the parent globule (i.e., Chernin & Masson 1991; Olberg et al. 1992; van Kempen et al. 2009). The protostellar wind's blueshifted (northeastern) lobe breaks out of the cloud, where there is little molecular gas for it to entrain, while the redshifted lobe dives into the globule and is able to entrain much more gas along its path.

In addition to the drastic difference in length, each lobe exhibits dissimilar morphologies most likely caused by differing dominant entrainment processes. The blue lobe shows mainly a parabolic morphology, with a P.A. of about 60°. The morphology and the velocity structure of the blue lobe suggests this molecular outflow is mostly being formed by the entrainment of cloud material by a wide-angle protostellar wind (see Section 4.1). We also detect in the blue lobe a small protuberance southeast of the continuum source (labeled B0 in Figure 1), which we argue is due to the outflow from a binary companion (see Section 4.4). The red lobe, on the other hand, has a V-shape near the source, with an opening angle of about 65°. Starting at about 30″ from the source, the integrated intensity contours mostly trace the southern and northern outflow cavity walls, which extend up to 80″ and 2′, respectively, from the source. We suspect that these structures trace the limb-brightened walls of an approximately cylindrical shell produced by the outflow–cloud interaction. In

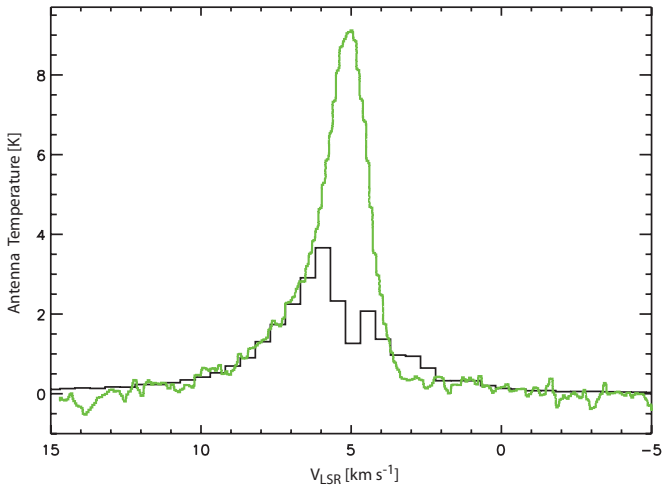


**Figure 2.** Comparison between CO(1–0) spectrum from Olberg et al. (1992) and our ALMA observations. The spectrum shown in green is the same one shown in Figure 4 of Olberg et al. (1992), which comes from the brightest position in the redshifted lobe of their the map. The black histogram shows the spectrum at the same position from a map using our ALMA data that have been smoothed to the same beam size as that of the Olberg et al. data (44″). The spectrum from the ALMA data is also smoothed to a velocity resolution of 0.5 km s$^{-1}$ for easier visual comparison with the Olberg et al. spectrum.

(A color version of this figure is available in the online journal.)

addition, we detect three distinct clumps of gas along the outflow axis which we label R1, R2, and R3 (see Figure 1). In Section 4.2, we argue that these result from approximately periodic mass ejections driven by the central protostar.

In Figure 2, we plot the spectrum at the position of brightest integrated intensity in the CO(1–0) outflow map of Olberg et al. (1992). We compare the spectrum shown in Figure 4 of Olberg et al. (1992) with a spectrum obtained from our CO map, smoothed to the same resolution as the beam size of the Olberg et al. observations (44″). From this comparison we see that the ALMA observations recover most (if not all) of the emission at LSR velocities greater than 6.5 km s$^{-1}$ and less than 3.5 km s$^{-1}$, and it is clear that we do not fully recover the emission at velocities close to that of the cloud ($v_{\rm LSR} \sim 5$ km s$^{-1}$, van Kempen et al. 2009). We are therefore confident that our ALMA data can be used to reliably study the emission at outflow velocities greater than about 1.5 km s$^{-1}$.

#### 3.2.1. Channel Maps

Figure 3 shows the emission over the outflow velocity range between approximately −6 and 6 km s$^{-1}$, and reveals how the CO emission structure of the region depends on velocity. We define outflow velocity ($v_{\rm out}$) as the LSR velocity of the emission minus the cloud LSR velocity. Panels in the upper row (blueshifted velocities) and lower row (redshifted velocities) present the emission averaged over a 1 km s$^{-1}$ range centered on the velocity indicated in the upper right corner of each panel. Panels in the center row show emission averaged over 0.5 km s$^{-1}$ wide range for velocities close to that of the cloud. We note that low-intensity outflow emission is detected at higher outflow velocities than those shown in Figure 3. This weak high-velocity emission is only seen when integrating the emission over a larger velocity range ($\gtrsim$5 km s$^{-1}$); see Sections 4.1 and 4.2.

In Figure 3, the first two panels in the upper row ($v_{\rm out} = -5.8$ and −4.8 km s$^{-1}$) show an approximately symmetric parabolic (low-intensity) structure extending northeast of the source. At lower blue outflow velocities, the emission is stronger and the northern wall of the lobe extends further from the source than the southern wall. At $v_{\rm out} = -2.8$ km s$^{-1}$ we detect two faint arcs of emission, about 40″ northeast and 2′ southwest of the protostar, which we ascribe to the limb-brightened edge of the host globule. These arcs are brighter closer to the cloud velocity (see panels at $v_{\rm out} = -0.1$ and 0.4 km s$^{-1}$). At $v_{\rm out} = -1.8$ km s$^{-1}$ the blueshifted outflow emission is very bright and it is concentrated in an inclined V-shape structure northeast of the source. It is only at very low outflow velocities that we detect the clump B0, about 20″ southeast of HH 47 IRS, which very likely traces the molecular outflow driven by the binary component that is not driving the main HH 46/47 outflow (see Section 4.4). In this panel we also detect faint emission southwest of the outflow source, coincident with some of the regions where we detect redshifted outflow emission. It is possible that the walls of the southwest (mainly redshifted) outflow lobe are expanding into the surrounding cloud (similar to the RNO 91 outflow; Lee & Ho 2005), and the filamentary blueshifted emission comes from the front walls of the cavity. In addition, at $v_{\rm out} = -1.8$ km s$^{-1}$ we detect a small relatively bright clump close to the position of the HH 47C shock (and the redshifted clump R3) at about 2′ southwest from the source, which most likely arises from gas entrained by HH 47C.

As shown in Figure 2, close to the cloud velocity our interferometer observations do not fully recover the emission from the cloud, as the observations are not sensitive to large-scale ($\gtrsim$20″) structures. This is the reason why the channel maps from $v_{\rm out} = -1.1$ to 0.9 km s$^{-1}$ appear so clumpy and the emission at these velocities cannot be used to obtain reliable estimates of the outflow or cloud mass nor to map the overall distribution of the cloud molecular gas. There are, however, a few small-scale features that are discernible among the clumpy mess. Even at $v_{\rm out} = -1.1$ km s$^{-1}$ we are able to identify the V-like structure just northeast of HH 47 IRS due to the blue outflow lobe, and a clump of gas close to the position of HH 47C. At the velocity of the cloud (i.e., the $v_{\rm out} = -0.1$ and 0.4 km s$^{-1}$ panels) we detect emission from the edge of the cloud, which is coincident with the diffuse 8 $\mu$m emission observed in *Spitzer Space Telescope* images of the region that borders the edge of the host globule (Noriega-Crespo et al. 2004; Velusamy et al. 2007). This structure seems to trace the outer parts of the cloud that are being heated by the UV radiation from the stars that produce the Gum Nebula. Acceleration of the gas at the globule's edge caused by a UV-radiation-induced photoablation flow could explain the fact that we detect the globule's edge at two different velocities separated by ∼3 km s$^{-1}$ (i.e., at $v_{\rm out} \sim 0$ and $v_{\rm out} \sim -3$ km s$^{-1}$). Certainly, a more detailed study of the cloud's kinematics is needed to understand the origin of the velocity structure at the globule's edge.

The $v_{\rm out} = 0.4$ km s$^{-1}$ panel also exhibits a bright structure that extends northeast of the source and coincides with the HH 46 optical nebula (see Section 4.1). This very low velocity emission could be due to the gas that is entrained by the expanding back wall of the northeast (mainly blueshifted) lobe. At $v_{\rm out} = 0.9$ km s$^{-1}$ the overall structure of the CO emission is similar to the integrated intensity image of the redshifted lobe in Figure 1, yet there are some notable differences. These include a bright narrow structure that extends northeast of the source (coincident with the blue lobe), and the fact that the wide-angle morphology of the southwest lobe is more prominent here than in the integrated intensity map (which we argue in Section 4.2 is evidence for the existence of a wide-angle wind).

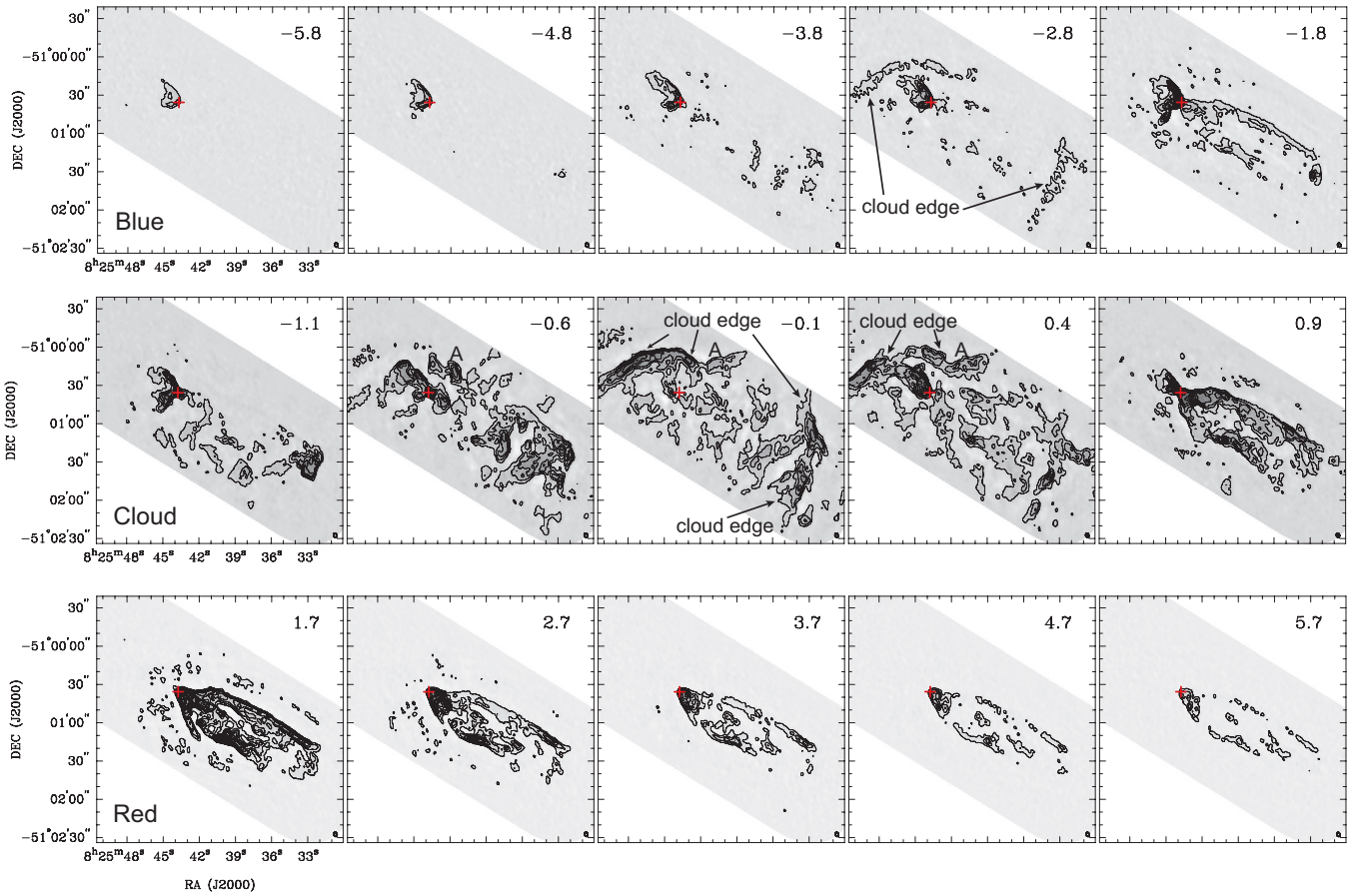


**Figure 3.** Channel maps of the CO(1–0) emission. Top (bottom) row shows blueshifted (redshifted) emission, where each panel shows the emission average over 1 km s$^{-1}$. The lowest contour and subsequent contour steps are 0.075 and 0.15 Jy beam$^{-1}$, respectively. The middle row shows velocities near the cloud velocity, and each panel shows the emission average over 0.5 km s$^{-1}$. The lowest contour and subsequent contour steps are 0.15 and 0.3 Jy beam$^{-1}$, respectively. The central outflow velocity is given in the upper right corner of each panel in units of km s$^{-1}$. The synthesized beam is shown on the lower right corner of each panel. The red cross shows the position of HH 47 IRS.

(A color version of this figure is available in the online journal.)

Similar to the blue lobe, the redshifted outflow lobe is brighter at lower outflow velocities. The $v_{\rm out} = 1.7$ km s$^{-1}$ panel shows the strongest emission, where the highest intensity is seen close to the source and on the southern and northern walls of the outflow lobe. In this panel the CO emission shows a wide-angle morphology close to the source, and the emission associated with the northern outflow wall is somewhat extended (as opposed to a simple narrow structure as seen at higher outflow velocities). The three redshifted clumps (R1, R2, and R3) are seen most clearly at $v_{\rm out} = 2.7$ and 3.7 km s$^{-1}$, but they are also detected out to $v_{\rm out} \sim 5$ km s$^{-1}$. The channel maps also show that from $v_{\rm out} = 1.7$ km s$^{-1}$ to $v_{\rm out} = 5.7$ km s$^{-1}$ the redshifted lobe becomes slightly narrower as the velocity increases.

### 3.2.2. Outflow Mass, Momentum, and Energy

To obtain a reliable estimate of the outflow mass we would need to know the opacity of the $^{12}$CO(1–0) line, as in outflows the opacity is expected to vary with velocity (Bally et al. 1999; Yu et al. 1999; Arce & Goodman 2001b). One way to estimate the opacity of the $^{12}$CO(1–0) line is using the ratio of $^{12}$CO(1–0) to $^{13}$CO(1–0). Unfortunately, there are no existing observations of the $^{13}$CO(1–0) emission with an angular resolution (and sensitivity) similar to our $^{12}$CO ALMA map that would allow us to properly correct for the opacity. We thus estimate the mass assuming the line is optically thin, and warn that our masses are very likely underestimated, by a factor of few or even as much as an order of magnitude (e.g., Cabrit & Bertout 1990; Arce & Goodman 2001b; Offner et al. 2011). We follow Bourke et al. (1997) to estimate the outflow properties from the CO(1–0) data, assuming an abundance ratio of $[^{12}{\rm CO}]/[{\rm H_2}] = 10^{-4}$, as in Olberg et al. (1992).

An estimate of the CO outflow excitation temperature is needed to calculate the outflow mass. However, there is a very wide range of temperature values given in the literature for the HH 46/47 molecular outflow. Chernin & Masson (1991) use the ratio of brightness temperature between the CO(3–2) and CO(2–1) at outflow velocities to estimate an outflow excitation temperature ($T_{\rm ex}$) of 8.5 ± 1 K (but use a value of 10 K in their outflow mass calculations). On the other hand, Olberg et al. (1992) estimate an excitation temperature, at outflow velocities, of 15 K using the intensity ratio of CO(1–0) to CO(2–1). van Kempen et al. (2009) use their multi-line observations to conduct a thorough and detailed study of the physical conditions of the gas surrounding HH 47 IRS, and estimate larger values for the outflow excitation temperature (between 50 and 150 K, but most likely about 100 K). Without ALMA observations of higher CO transition lines we cannot make our own detailed map of $T_{\rm ex}$, with an angular resolution comparable to our CO data, along the entire extent of the outflow. Therefore, we calculate the outflow mass, and other outflow properties shown in Table 1, using different values of excitation temperature. It is clear that

**Table 1**
Outflows Properties

| Lobe | | Mass[a] ($10^{-2}$ $M_\odot$) | | | Momentum[a, b] ($10^{-2}$ $M_\odot$ km s$^{-1}$) | | | Energy[a, b] ($10^{42}$ erg) | | |
|---|---|---|---|---|---|---|---|---|---|---|
| | $T_{ex}$ = | 15 K | 50 K | 100 K | 15 K | 50 K | 100 K | 15 K | 50 K | 100 K |
| Blue | | 1 | 2 | 3 | 3/6 | 8/16 | 15/30 | 3/12 | 8/32 | 14/56 |
| Red | | 3 | 8 | 14 | 12/24 | 27/54 | 51/102 | 9/36 | 21/84 | 39/156 |

**Notes.**
[a] Estimates are obtained assuming emission is optically thin. Values should be treated as lower limits.
[b] Values before the slash are not corrected for the outflow inclination and those after the slash are corrected assuming an inclination of the outflow axis, with respect to the plane of the sky, of 30°.

uncertainties in $T_{ex}$ result in highly inaccurate estimates of the outflow properties. We note that if we consider the same excitation temperature and the same velocity ranges used by Olberg et al. (1992) for the two different outflow lobes (i.e., $T_{ex}$ = 15 K, $v_{out}$ = −5.0 to −1.5 km s$^{-1}$ for the blue lobe and $v_{out}$ = 1.5–7.5 km s$^{-1}$ for the red lobe), we obtain a total outflow mass of $3.6 \times 10^{-2}$ $M_\odot$, similar to the value of 0.03 $M_\odot$ obtained by Olberg et al. This is consistent with Figure 2, which shows that our interferometric observations recover most (if not all) of the emission at outflow velocities greater than 1.5 km s$^{-1}$.

Our observations are much more sensitive than any previous study of the HH 46/47 molecular outflow, which allows us to detect outflow emission over a much wider velocity range. In this work we measure the outflow mass ($M_{out}$), momentum [$P_{out} = \Sigma M_{out}(v_{out})v_{out}$], and energy [$E_{out} = 0.5\Sigma M_{out}(v_{out})v_{out}^2$] over the velocity range where we detect outflow emission with intensity greater than $3\sigma$, that is $-30$ km s$^{-1}$ $< v_{out} <$ $-1.6$ km s$^{-1}$ for the blue lobe and 1.4 km s$^{-1}$ $< v_{out} <$ 40 km s$^{-1}$ for the red lobe (see Table 1). In both lobes the very high velocity outflow ($|v_{out}| > 20$ km s$^{-1}$) is constrained to within about 15″ of the source. Detection of low-intensity CO(1–0) outflow emission at very high velocities resulted in our estimates of the outflow kinetic energy and momentum to be significantly higher than those of Olberg et al. (1992). This implies that other similar molecular outflows may be much more energetic than what previous (low-sensitivity) observations indicated and outflows may have the potential to have more impact on their surrounding cloud than previously thought.

We can compare the properties of the jet with those of the molecular outflow in order to investigate whether the jet injects enough momentum into the cloud and drives the molecular outflow. Assuming $T_{ex}$ = 50 K, the momentum of the red lobe is ∼0.5 $M_\odot$ km s$^{-1}$ (see Table 1). The mass loss rate of the HH 47 jet (inward of HH 47A) was estimated by Hartigan et al. (1994) to be about $4 \times 10^{-7}$ $M_\odot$ yr$^{-1}$. Using a jet velocity of 300 km s$^{-1}$ (see above), the momentum rate in the jet is then estimated to be $1.2 \times 10^{-4}$ $M_\odot$ km s$^{-1}$ yr$^{-1}$. We adopt the age of the wind to be 9000 yr, the dynamic age of the parsec-scale HH flow associated with HH 46/47, discovered by Stanke et al. (1999). Assuming the red lobe has a similar momentum rate as the blue lobe and that the rate has been approximately constant over the lifetime of the flow, we estimate that the jet has been able to inject a total of about 1 $M_\odot$ km s$^{-1}$ into the surrounding medium, which could be enough to drive the molecular outflow (if the assumptions above are correct). However, it should be kept in mind that our estimate of the molecular outflow momentum is probably underestimated by a factor of a few to possibly an order of magnitude (since we assumed the emission is optically thin). Moreover, if we instead use the dynamic age of the jet within the globule (using the size of the jet comparable to the molecular outflow red lobe), that is ∼1000 yr, the estimated momentum injected by the jet into the cloud would be approximately 0.1 $M_\odot$ km s$^{-1}$. It thus seem that there is material ejected by the protostar which is not detected in the optical or IR—and therefore not included in the estimate of the jet mass loss rate quoted above—that contributes to the momentum injected by the protostellar wind into the cloud that drives the molecular outflow.

## 4. DISCUSSION

### 4.1. Blue Lobe: Evidence for Wide-angle Wind

As mentioned above, we detect blueshifted outflow emission out to larger velocities than what is presented in Figure 3. The intensity of the high-velocity emission is very low and it is necessary to sum over velocity ranges wider than 1 km s$^{-1}$ in order to detect significant emission. In Figure 4, we show four velocity maps, integrated over different velocity ranges, that show the morphology of the high-velocity blue lobe gas. From this figure, it is clear that at higher outflow velocities the emission extends farther from the source, compared to lower velocities. In addition, in panels (b)–(d) the emission shows an elongated ring or shell-like structure. This general behavior, in both morphology and velocity distribution, is consistent with the expected properties of a molecular outflow entrained by a wide-angle wind (Shu et al. 1991; Lee et al. 2000; Arce & Goodman 2002).

In order to further investigate the underlying protostellar wide-angle wind and entrainment mechanism in the blue lobe, we constructed a position–velocity ($p$–$v$) diagram along the axis of the outflow, shown in Figure 5. This figure shows an inclined parabolic structure, as expected for an outflow entrained by a wide-angle wind with a non-zero inclination of the outflow axis with respect to the plane of the sky (Lee et al. 2000, 2001). The relatively high angular resolution and sensitivity of our ALMA data results in one of the most (if not the most) clear case where such a parabolic structure is detected in the $p$–$v$ diagram of a molecular outflow lobe.

We follow the simple analytical model by Lee et al. (2000) to describe the blue lobe of the HH 46/47 molecular outflow. In this model, which is based on the study by Li & Shu (1996), the molecular outflow is made up of the gas that is swept up by a wide-angle wind that propagates into a flattened (toroid-like) dense core. The resulting molecular outflow can then be modeled by a radially expanding parabolic shell with a velocity structure in which velocity increases with distance (i.e., a Hubble law velocity structure). A diagram of the model is shown in Figure 21 of Lee et al. (2000), and in cylindrical coordinates (with the $z$-axis along the symmetry axis of the wind and the $R$-axis perpendicular to it) the morphology of the shell can be represented by the equation $z = CR^2$, while the velocity components of the shell along the $z$ and $R$ axes are represented

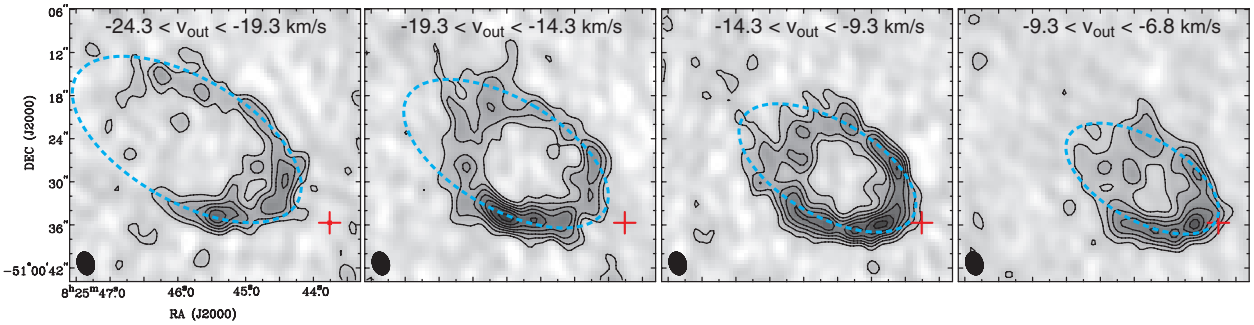


**Figure 4.** Velocity range-integrated intensity maps of the CO blueshifted emission. The velocity interval of integration is given on the top of each panel. In all panels, the lowest contour and contour steps are 0.07 Jy beam$^{-1}$ km s$^{-1}$. The dashed blue ellipse in each panel shows the expected shape of the molecular outflow shell driven by a wide-angle wind using the model described in the text (see Section 4.1). The model shell is calculated using the outflow velocity at the center of the velocity interval of integration, and the same parameters used to model the $p$–$v$ diagram in Figure 5. The synthesized beam is shown in the lower left corner of each panel. The red cross shows the position of HH 47 IRS.

(A color version of this figure is available in the online journal.)

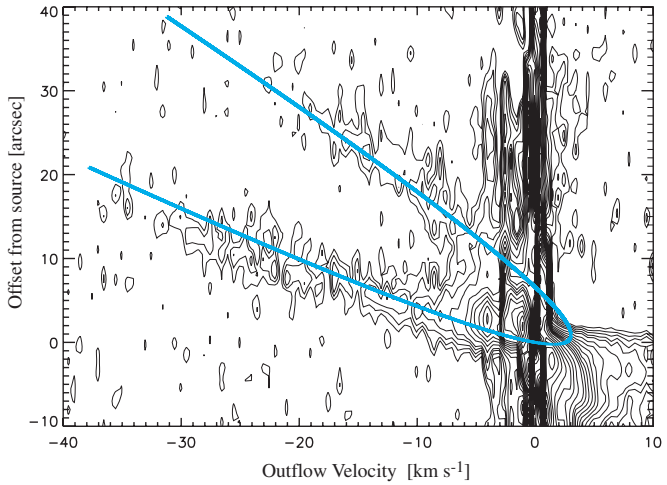


**Figure 5.** Position–velocity diagram along the axis of the blue lobe. The figure was constructed using a map with velocity resolution of 0.5 km s$^{-1}$, and summing the emission over a 7.″5 (about three beams) wide cut, with a position angle of 60°. Contours have values of 0.35, 0.66, 1, 1.5, 2, and 3 Jy beam$^{-1}$, and subsequent steps of 1 until 10 Jy beam$^{-1}$, and thereafter in steps of 2 Jy beam$^{-1}$. The light blue parabola shows the model fit to the data (see Section 4.1).

(A color version of this figure is available in the online journal.)

by $v_z = v_o z$, $v_R = v_o R$. In these equations $C$ and $v_o$ are free parameters with units of arcsec$^{-1}$ and km s$^{-1}$arcsec$^{-1}$, which are constrained by the shape of the molecular outflow shell and the shape of the $p$–$v$ diagram, respectively.

A map of the high-velocity blue lobe parabolic structure was produced by integrating the emission for outflow velocities between −26 and −4 km s$^{-1}$, in order to avoid "contaminating" emission from the cloud and the binary component outflow (see Figure 3). We rotated the map by −30° and fit a parabola ($z = CR^2$) to the structure. The fit gives a value for $C$ of $0.3 \pm 0.05$, where the errors indicate the range of values that provide a reasonable fit to the map. We then fit the $p$–$v$ diagram with the wide-angle wind model of Lee et al. (2000) described above. We constrain the inclination angle with respect to the plane of the sky ($i$) to 30° ± 10°, close to the values derived by Eislöeffel & Mundt (1994) and Hartigan et al. (2005), assuming a distance to the parent globule of 450 pc. We find that a value of $v_o = 2.3 \pm 0.2$ km s$^{-1}$ arcsec$^{-1}$ and a value of $i = 29° \pm 1°$ result in a reasonable fit to the $p$–$v$ cut. The errors indicate the range of values for which reasonable fits are attained, and choosing significantly different values for these two parameters would result in a parabolic curve with a different width or inclination compared to the $p$–$v$ diagram obtained from our data.

The wide-angle wind model can also be used to predict the shape of the molecular outflow shell at different velocities (Lee et al. 2000; Hirano et al. 2010). We used the parameters derived above, and plot the predicted shape at different outflow velocities in Figure 4. For each panel the dash ellipse shows the expected shape of the molecular outflow shell, according to the wide-angle wind model, at the outflow velocity at the center of the velocity interval of integration (shown at the top of each panel). The model provides a reasonable match to the velocity range-integrated intensity maps, as the observed emission structure follows the general trend expected from the model. That is, at lower outflow velocities the outflow shell is more compact and its southwestern end coincides with the position of the source, while at higher velocities the shell is more extended and lies further away from the source.

This simple analytical model is probably not the only model that may reproduce the observed morphology. For example, in a jet (or collimated wind) with varying ejection velocity, such as HH 46/47 (e.g., Raga et al. 1990), fast-moving ejecta can collide with previously ejected (slower-moving) material. As a result of such collisions the wind material may expand and push ambient material in a direction perpendicular to the jet axis, possibly creating a wide cavity with low collimation (e.g., Suttner et al. 1997; Cabrit et al. 1997). However, the fact that we can reasonably fit the velocity range-integrated intensity maps (Figure 4) and the $p$–$v$ diagram (Figure 5) with the wide-angle wind model described above suggests that the observed blue lobe could very likely have been formed by the entrainment of a wide-angle wind and the ambient cloud. Our data, however, cannot distinguish between possible wind-launching mechanisms that can produce wide-angle winds (e.g., X-wind, Shang et al. 2006 or disk winds, Pudritz et al. 2006). We would need higher angular resolution data to probe down to less than ∼50 AU from the source in order to possibly discriminate between different launching mechanisms (e.g., Ferreira et al. 2006).

It might seem conflicting that the blue outflow lobe appears to be entrained by a wide-angle wind, when it is coincident with the base of a well-studied jet (see Figure 6). However, it is possible for both a collimated wind component (i.e., a jet) to coexist with a wide-angle wind (see, e.g., models by Shang et al. 2007; Pudritz et al. 2007; Fendt 2009; Tomida et al. 2013). In fact, this is not the first source to exhibit such characteristics. Three

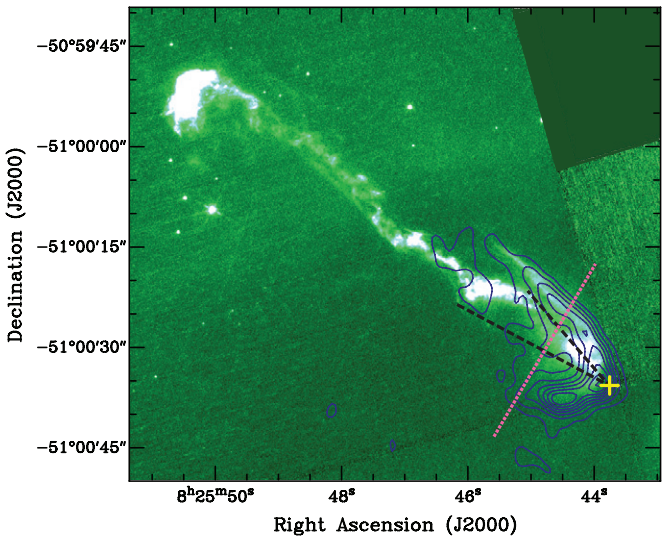


**Figure 6.** Comparison of blue CO lobe and optical image of HH 46/47 jet. The *HST* image was taken with the [S II] (F673N) filter in 2008 by Hartigan et al. (2011). Contours show the emission integrated over the velocity range from −6.8 to −3.2 km s$^{-1}$. This velocity range was chosen to avoid contamination from cloud emission and B0. The lowest contour and subsequent contour steps are 0.15 and 0.2 Jy beam$^{-1}$ km s$^{-1}$, respectively. The yellow cross shows the position of HH 47 IRS. The two black dash lines connect the position of the source to outermost positions of the wiggling jet, with respect to the outflow axis. The dotted pink line perpendicular to the outflow cavity shows the position of the $p$–$v$ cut shown in Figure 10(a).

(A color version of this figure is available in the online journal.)

examples where a "dual-component" wind have been invoked to explain the mm and optical/IR outflow observations are HH 111 (Nagar et al. 1997, Lee et al. 2000, however see Lefloch et al. 2007 for an alternative explanation), HH 315 (Arce & Goodman 2002), and B5-IRS 1 (Yu et al. 1999). In the first two cases the protostellar source is close to the cloud edge, the blue optical jet (or HH flow) is clearly seen to reside outside the dense parts of the cloud, and the morphology of the molecular outflow's blue lobe is consistent with it being formed by a wide-angle wind (similar to HH 46/47). This is possible if the underlying protostellar wind has both a collimated (jet) and a wide-angle component and the gas in the blue lobe is mostly entrained by the wide-angle component. The reason that the wide-angle wind dominates the gas entrainment in these sources (including HH 46/47) is possibly due to the fact that the jets lie in a region of very low density molecular gas, on the outskirts of the cloud. Numerical simulations of jet shock-driven outflows show that most of the gas entrainment takes place at (or near) the head of the bow shock (e.g., Smith et al. 1997; Lee et al. 2001), while in a radially expanding wide-angle wind entrainment mostly takes place in a wide-angle shell originating at the source. Hence, in a dual-component wind where the jet bow shocks mostly reside outside the cloud, the circumstellar molecular gas will mostly be accelerated by the wide-angle wind component close to the source, where there is enough molecular material for the wind to entrain and form the observed molecular outflow.

Further evidence that the blue lobe of the HH 46/47 molecular outflow is entrained by a dual-component wind is observed by comparing the morphology of the blueshifted gas and that of the optical jet. In Figure 6, we show contours of the low-velocity blueshifted lobe plotted over the *HST* image of the HH 47/46 jet. The northern wall of the CO blue lobe follows the northern edge of the optical nebula, which implies that the bright parabolic structure observed in CO traces the walls of the outflow cavity. The jet's wiggling structure suggests that the jet axis changes with time or precesses (i.e., Reipurth et al. 2000). In Figure 6, we show the opening angle of the precession cone in the plane of the sky, delimited by lines that connect HH 47 IRS and the bright emission knots at the most extreme angles with respect to the protostellar source. It is clear that the opening angle of the molecular outflow lobe is substantially wider than that of the jet precession cone. It is therefore highly unlikely that precession of the jet alone could, by itself, produce the wide-angle cavity traced by the CO outflow.

### 4.2. Red Lobe

Compared to the blue lobe, the red lobe of the HH 46/47 molecular outflow exhibits a more complex spatial and kinematical structure. In Figure 7, we show maps of the redshifted outflow emission integrated over different velocity ranges chosen to highlight the different important structures discernible at different velocities. These are discussed in detail below.

#### 4.2.1. Morphological Evidence for the Existence of a Wide-angle Wind

Figure 7(a) presents a map of the low outflow velocity emission ($1.2 < v_{\rm out} < 2.7$ km s$^{-1}$), where the lobe shows a clear wide-angle structure, with an opening angle of 65°,

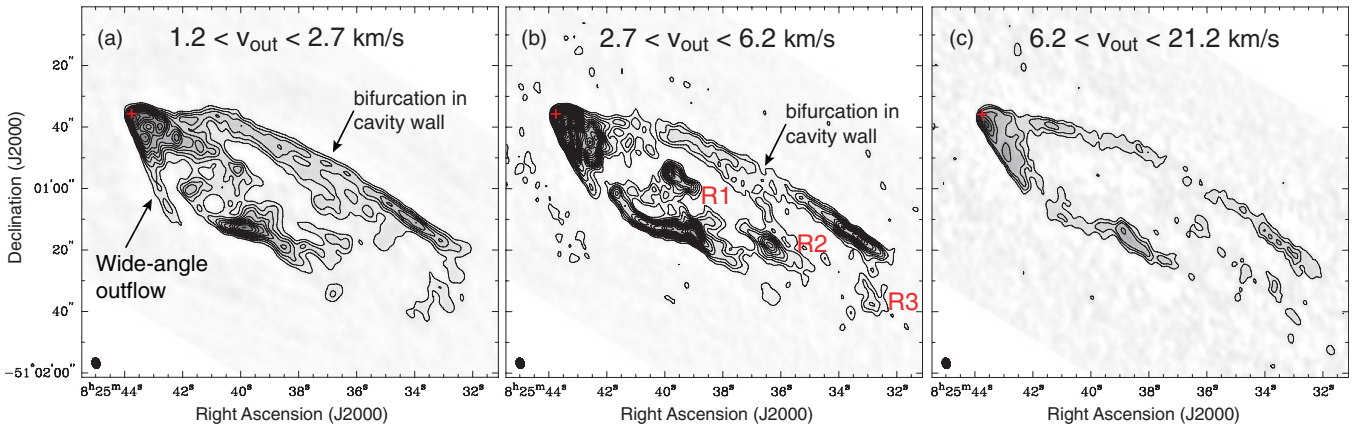


**Figure 7.** Velocity range-integrated intensity maps of the CO redshfited emission. The velocity interval of integration is given at the top of each panel. In the left, middle, and right panels the lowest contour and contour steps are 0.2, 0.105, and 0.2 Jy beam$^{-1}$ km s$^{-1}$, respectively. The synthesized beam is shown on the lower left corner of each panel. The red cross shows the position of HH 47 IRS.

(A color version of this figure is available in the online journal.)

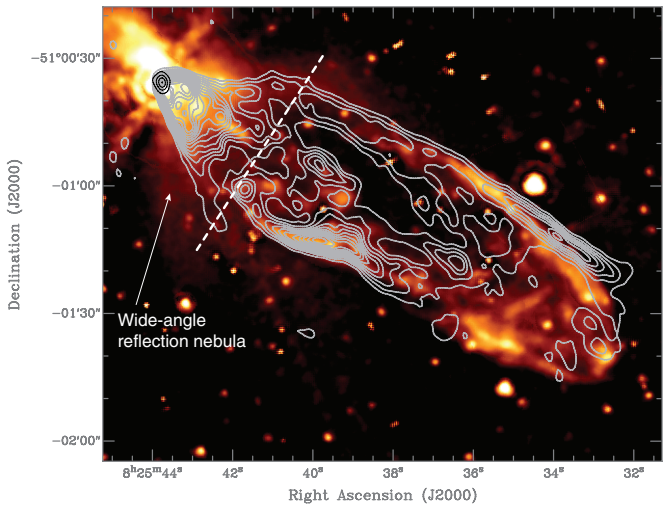


**Figure 8.** Comparison of red CO lobe with *Spitzer* IRAC 2 (4.5 $\mu$m) image. The *Spitzer* data are from Noriega-Crespo et al. (2004) and have been reprocessed with a deconvolution algorithm to reach an angular resolution of ∼0.″6–0.″8, with 60 iterations (see Noriega-Crespo & Raga 2012 for details). Gray contours show the integrated intensity of the CO redshifted lobe (the same as shown in Figure 1). Black contours show the 3 mm continuum emission around HH 47 IRS. The lowest contour and subsequent contour steps are 2 mJy beam$^{-1}$. The white dashed line shows the position of the $p$–$v$ cut shown in Figure 10(b).

(A color version of this figure is available in the online journal.)

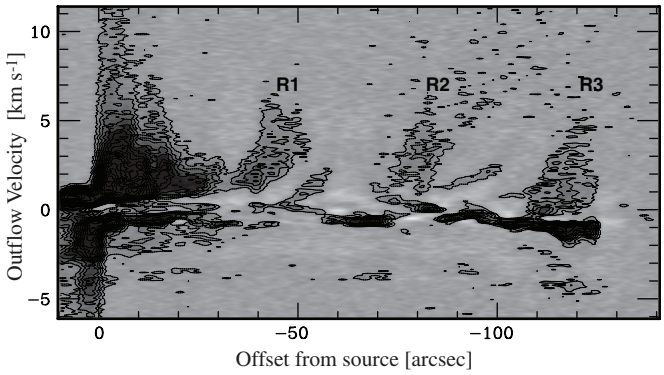


**Figure 9.** Position–velocity diagram along the axis of the red lobe. The figure was constructed using a map with velocity resolution of 0.08 km s$^{-1}$, with a position angle of 60°, and summing the emission over a 7.″5 wide cut. The lowest contour and subsequent contour steps are 1 and 1.5 Jy beam$^{-1}$, respectively. The positions of the redshifted outflow clumps along the outflow axis are shown.

**Table 2**
Properties of Clumps in Redshifted CO Outflow Lobe

| Clump | Distance from Source[a] | | Age[a] | Mass[b] |
|---|---|---|---|---|
| | (arcsec) | (pc) | (yr) | ($10^{-3}$ $M_\odot$) |
| R1 | 42 | 0.1 | 360 | 2.1 |
| R2 | 81 | 0.2 | 650 | 1.8 |
| R3 | 118 | 0.3 | 945 | 0.7 |

**Notes.**
[a] Values of linear distance and age have been corrected for the inclination of the outflow axis, assuming $i = 30°$.
[b] Mass estimate obtained assuming optically thin emission and an excitation temperature of 50 K. Values shown should be treated as lower limits.

within 40″ of the source. This wide-angle structure is drastically different from the morphology of the bright IR outflow cavity walls seen in the IRAC *Spitzer* observations (Noriega-Crespo et al. 2004), which is similar to the structure of the CO outflow red lobe at distances from the source further than 40″ (see Figure 8). The loop-like structure seen in the IRAC images has been adequately modeled as the cavity walls of a jet-driven outflow by Raga et al. (2004). This model, however, does not reproduce the wide-angle structure seen in low-velocity CO emission nor the wide-angle IR nebula seen close to the source in re-processed IRAC images of HH 46/47 (see below). It seems, therefore, that the wide-angle structure is not produced by the collimated (jet) component responsible for the bright outflow cavity walls seen both in CO and IR, extending form about 30″ to 2′ away from the source. Similar to the blue lobe, the red lobe shows evidence of both a collimated and a wide-angle wind component.

Recently, Velusamy et al. (2007) presented reprocessed images of the IRAC observations of HH 46/47, which included suppression of side lobes from bright sources and enhanced resolution (compared to the images presented by Noriega-Crespo et al. 2004). The 3.6 and 4.5 $\mu$m images show diffuse and extended emission close to the source with a parabolic morphology, with an opening angle of about 110°, which Velusamy et al. (2007) argue is due to scattered light arising from a wide-angle outflow cavity (see Figure 8). This structure is wider than the CO outflow lobe, and we suspect we are not able to trace the full extent of the IR reflection nebula due to the high opacity of the CO(1–0) at velocities close the ambient cloud. In the few cases where a molecular outflow has been mapped in $^{13}$CO, it typically shows a wider opening angle (at lower outflow velocities) than the lobe traced by the $^{12}$CO emission and the optical/IR reflection nebula (i.e., Ohashi et al. 1997; Tafalla & Myers 1997; Arce & Sargent 2006). We expect that future observations using lines with a lower opacity (or that probe higher densities) will be able to trace the wide-angle cavity outlined by the faint extended IR emission.

#### 4.2.2. Evidence for Episodic Mass Ejections

Among the most distinct structures in the velocity-integrated map shown in Figure 7(b) are three bright and compact features along the outflow axis. These local maxima of emission are the same clumps identified in Figure 1 as R1, R2, and R3. They are more clearly seen in Figure 7(b) because of the limited velocity range used to produce this figure compared to Figure 1. Table 2 shows the distance from the source as well as other physical properties of each of the molecular clumps. The distance from the source to R1 (about 0.1 pc) is approximately equal to the distance between R1 and R2, and the distance between R2 and R3. This suggests they might be the result of periodic ejection episodes, similar to those found in other molecular outflows (e.g., L1448, Bachiller et al. 1990; RNO 43, Bence et al. 1996; HH 300, Arce & Goodman 2001b). In fact, R1 and R2 are at similar distances from HH 47 IRS as the bright bow-shock structures HH 47B and HH 47A, respectively, along the optical jet, in the opposite (blue) lobe of HH 46/47. These two HH knots are thought to arise from different mass ejection episodes (Reipurth & Heathcote 1991), and the R1 and R2 clumps may be associated with the counterejections (in the redshifted lobe) of the mass-loss events that caused HH 47B and HH 47A. Similarly, R3 is coincident with HH 47C (in the red lobe), which is thought to be associated with the ejection responsible for the HH 47D bow shock (in the blue lobe).

To further investigate the nature of the outflow clumps we show, in Figure 9, a $p$–$v$ diagram along the axis of the redshifted molecular outflow lobe. At distances greater than 30″ from the source, the $p$–$v$ diagram shows three regions where there is a clear increase in the outflow velocity coincident with the

position of the red outflow clumps. These features in the $p$–$v$ diagram, generally referred to as "Hubble wedges" (Arce & Goodman 2001a), show maximum outflow velocity increasing as a function of distance from the source, within a localized length along the outflow axis. The general consensus is that such features are formed by a collimated (jet-like) episodic flow with a significantly varying mass-ejection rate, where each clump associated with a Hubble wedge is produced by the bow-shock entrainment of an individual mass-ejection event (Arce & Goodman 2001a; Lee et al. 2001). That is, each clump is mostly made of ambient gas that has been swept up and accelerated by a protostellar wind ejection episode.

In Table 2, we list estimates of the timescale (i.e., age) for each mass ejection episode in HH 46/47 assuming that all clumps are moving away from the source at a constant space velocity. We expect the ejected material will decelerate as it moves through the cloud and interacts with the surrounding medium, which will result in slower velocities for older ejected material (e.g., Cabrit & Raga 2000; Goodman & Arce 2004). Yet, we can use an average flow velocity of the jet ($\bar{v}_{\rm jet}$) for all outflow clumps to obtain an estimate of the ejection age for each mass ejection episode. Existing studies indicate that $\bar{v}_{\rm jet} \sim 300$ km s$^{-1}$ for HH 46/47 (Eislöeffel & Mundt 1994; Micono et al. 1998; Hartigan et al. 2005). Using this velocity, we estimate that a major mass ejection event in HH 46/47 takes place approximately every 300 yr, consistent with the results from studies of the optical (blueshifted) jet.

The CO outflow clumps we detect are most likely made of gas that has been entrained near the current position of the clump. Observations indicate that the outflow mass rate in HH 46/47 is of the order of $10^{-7}\,M_{\odot}$ yr$^{-1}$ (Hartigan et al. 1994; Antoniucci et al. 2008; Garcia Lopez et al. 2010). From the length of R2 along the outflow axis (i.e., $\sim$20″), and assuming a constant $v_{\rm jet} = 300$ km s$^{-1}$, we estimate that the episodes of high-mass ejection last about $10^2$ yr. With the mass outflow rate given above this would result in a total of $\sim 10^{-5}\,M_{\odot}$ ejected in the wind, which is about two orders of magnitude less than the estimated gas mass of R2. The mass loss rate during the episode associated with R2 would have to be about two orders of magnitude higher than the rates estimated for HH 46/47 for the protostellar wind mass to be similar to the estimated gas mass of R2. Hence, it seems more likely that the vast majority of the detected molecular gas in the redshifted outflow clumps is cloud material that has been entrained by the protostellar wind rather than material from the protostellar wind itself.

Episodes of enhanced mass outflow rate are thought to be caused by an increase in the mass accretion rate onto the protostar. In the case of HH 46/47, there seems to be a mechanism that is able to produce an enhancement in the accretion rate every few hundred years. This timescale is significantly shorter than the estimated orbital period of the binaries in the HH 47 IRS system (see Reipurth et al. 2000). This rules out triggering of gravitational instabilities in the circumstellar disk of the source that drives the HH 46/47 outflow by the close passage of the known binary companion as a mechanism for enhanced disk accretion. A closer (yet unobserved) companion would have to exist for companion–disk interactions (Reipurth 2000) to be a feasible mechanism for triggering episodic mass ejections. Other mechanisms that could produce episodic accretion (and hence mass ejection) events have been discussed in the literature, where disk instabilities are the main cause of enhanced accretion events (e.g., Vorobyov & Basu 2005; Zhu et al. 2010; Machida et al. 2011). In many of the models the timescales between successive episode may be very different depending on the assumed input parameters, and in some of these models successive events of high-mass accretion rate can occur on timescales as low as a few 100 yr to about $10^3$ yr, consistent with the observed properties of the HH 46/47 outflow. Future studies of outflow episodicity using a large sample may help constrain variable accretion models.

Another morphological feature detected in the redshifted molecular outflow lobe that may be caused by multiple mass ejections is the bifurcation of the northern cavity wall. This feature is seen at low and medium outflow velocities (Figures 7(a) and (b)) at about 1′ away from the protostar along the northern wall of the outflow lobe. Here, the wall appears to divide into two filaments: a bright component that extends southwest approximately parallel to the outflow axis (P.A. $\sim -120^{\circ}$) and a fainter component that makes a sharp southward turn toward the position of R2 (see Figures 7(a) and (b)). Models and simulations of molecular outflows formed by episodic winds show that a thin shell or a cavity is formed around each internal bow shock formed by different ejection episodes (Gueth et al. 1996; Lee et al. 2001). We thus surmise that the filamentary feature that connects R2 and the northern wall of the red lobe traces the shell formed by the interaction of the ejection episode associated with R2 and the ambient gas. Faint emission connecting R1 to the southern wall of the lobe may indicate that a similar structure is also driven by R1.

#### 4.2.3. High-velocity Redshifted Emission

Figure 7(c) shows a velocity-integrated map over high CO outflow velocities in the red lobe ($6.2 < v_{\rm out} < 21.2$ km s$^{-1}$). Here, the outflow opening angle near the source ($\sim 50^{\circ}$) and the lobe width are smaller than at low outflow velocities. The overall arc-like morphology of the northern wall is consistent with the shape expected for an outflow lobe formed by (jet) bow-shock entrainment (e.g., Raga & Cabrit 1993; Lee et al. 2001). This and the other morphological and kinematical features discussed above imply that the dominant entrainment mechanism of the CO outflow observed beyond 40″ arises from a collimated episodic wind with a series of bow shocks along the axis. On the other hand, near the source, and at low outflow velocities the molecular outflow appears to have been formed by the entrainment from a wide-angle wind. A possible explanation is that the wide-angle component has a lower velocity (and possibly a lower density) than the collimated (jet-like and episodic) component. Near the source, where the ambient density is high, both the wide-angle and collimated component will entrain the gas, but the effects of the wide-angle wind will be seen most clearly at low outflow velocities and at relatively large angles away from the outflow axis. The faster moving (and denser) collimated component is able to travel further away from the source (and even puncture out of cloud near the position of R3), and thus the CO outflow further out from the source (and at high velocities) will exhibit properties of it being mostly entrained by a collimated wind. Certainly, a successful model for the HH 46/47 molecular outflow would need to reproduce the difference in morphology between the low and high outflow velocities and at different distances from the source.

### 4.3. Velocity Gradients in Outflow Cavity

The high-sensitivity, high-velocity resolution data allowed us to study the kinematics of the outflow cavity in detail. In

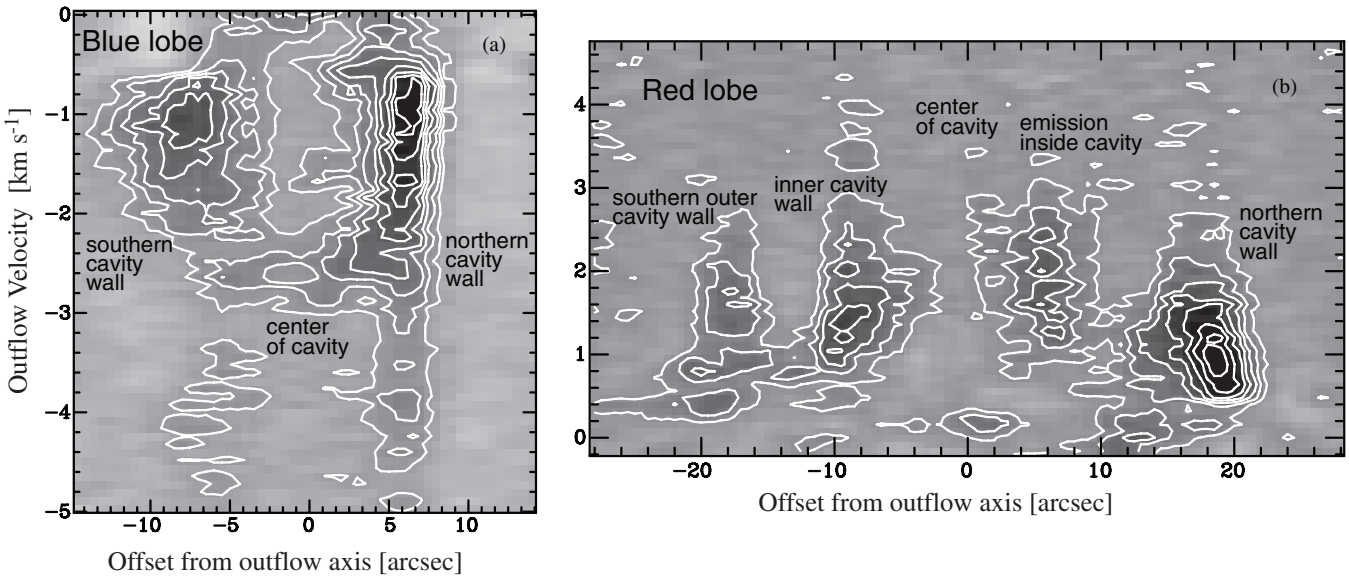


**Figure 10.** Position–velocity diagrams perpendicular to the outflow axis for the blue (left panel) and red (right panel) lobes. In both $p$–$v$ diagrams, the offsets are given with respect to the position of the outflow axis in the cut. The location of the $p$–$v$ cuts for the blue and red lobes are shown in Figures 6 and 8, respectively. In the left panel the lowest contour and the subsequent contour steps are 0.2 and 0.15 Jy beam$^{-1}$, respectively. In the right panel the lowest contour and the subsequent contour steps are 0.07 and 0.16 Jy beam$^{-1}$, respectively.

Figure 10, we plot the $p$–$v$ diagrams made by cuts perpendicular to the outflow cavities of the blue and red lobes. The figure shows that for both cavities there is a wide range of velocities present at the position of the cavity walls, and a gradual velocity gradient with most emission near the outflow axis at higher velocities than (most of) the emission closer to the outflow walls. In the blue lobe, at the position of the outflow cavity walls, there is detectable CO at velocities from $v_{\rm out} \sim -5$ km s$^{-1}$ to $v_{\rm out} \sim -0.5$ km s$^{-1}$. Yet, most of the emission at these position is at velocities close to that of the ambient cloud (i.e., between $v_{\rm out}$ of about $-2$ and $-0.5$ km s$^{-1}$; see Figure 10(a)). This is in contrast to positions closer to the outflow axis, where the bulk of the emission is at slightly higher velocities, between $v_{\rm out}$ of $-2$ and $-3$ km s$^{-1}$. A similar velocity distribution, but with much faster velocities, has been observed in the HH 46/47 optical jet with fast radial velocities ($\sim -100$ to $-150$ km s$^{-1}$) in the jet core and slower velocities ($\sim -25$ to $-50$ km s$^{-1}$) at the edges (Morse et al. 1994). In the CO outflow red lobe we see a spread in velocities (i.e., emission over a range of $v_{\rm out}$ of about 2 km s$^{-1}$) at the position of the cavity walls (and in the emission inside the outflow cavity), as well as an increase in the average (and minimum) velocity of the CO as the distance to the center of the cavity decreases: from an average velocity close to that of the ambient cloud ($v_{\rm out} \sim 0.5$ km s$^{-1}$) at the outer cavity wall, to an average $v_{\rm out} \sim 2$ km s$^{-1}$ at center of the outflow lobe (see Figure 10(b)).

The wide spread in velocities at the position of the cavity walls may be explained by both geometric effects and the expected interaction between the outflow and the surrounding cloud. Observations with limited angular resolution are expected to detect a large range in radial velocities (i.e., the component of the gas velocity along the line of sight) at the limb-brightened edge of an expanding parabolic (or cylindrical) cavity, as outflow gas from the front and back side of the cavity wall should contribute to the total detected emission. In addition, given that the cavity wall is where the outflow–cloud interaction takes place, one would expect the gas to be more turbulent here than close to the cavity center, and hence show a wider spread in velocities.

It is not clear what causes the observed velocity gradient perpendicular to the outflow axis. The decrease in velocity of about 1–2 km s$^{-1}$ from the center of the cavity to the cavity walls may be due to different processes. One possibility is that this behavior in the CO outflow results from the entrainment of a protostellar wind that has higher velocities toward the wind axis. For example, a disk wind where the velocity of the wind depends on the radius at which is launched (Pudritz et al. 2006) or a jet made of many small bow shocks where the entrained material at the head of the bow shocks (along the center of the jet) is expected to have higher velocities than the material entrained at the side wings of the bow shock (Heathcote et al. 1996). Another alternative is that the velocity gradient results from the momentum-conserving wind entrainment that produces the molecular outflow, where lower CO outflow velocities are expected in denser regions near the cavity walls (e.g., Arce & Sargent 2004). An additional possibility is that this is an effect due to the geometry of an expanding parabolic, conical, or cylindrical cavity inclined with respect to the plane of the sky. Undoubtedly, the detected gradient is not due to outflow rotation, as it has been recently claimed for a few other sources (e.g., Lee et al. 2009; Zapata et al. 2010; Choi et al. 2011; Pech et al. 2012). The observed decrease in velocity from the outflow axis toward the cavity walls is in contrast with the expected observational signatures of outflow rotation: a gradient across the entire lobe length with one side of the lobe showing bluer (or redder) velocities with respect to the other side of the lobe (e.g., Launhardt et al. 2009).

### 4.4. Outflow from Binary

As described in Section 3.2.1, the channel maps show a protuberance extending about 20″ southeast of the source, at low blueshifted outflow velocities ($v_{\rm out} \sim -1.8$ km s$^{-1}$). We believe that this clump (which we name B0) is not related to the main blueshifted outflow lobe, as it does not follow the general parabolic shape seen at most blueshifted velocities. A $p$–$v$ diagram oriented along a line from HH 47 IRS to B0, at

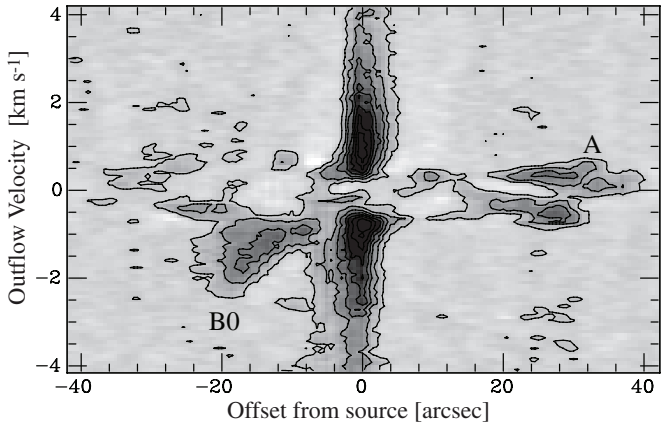


**Figure 11.** Position–velocity diagram along the axis of the proposed outflow powered by the binary companion in the HH 47 IRS system not responsible for the main HH 46/47 outflow. The location of the $p$–$v$ cut is shown in Figure 1. The lowest contour and the subsequent contour steps are 0.1 and 0.3 Jy beam$^{-1}$, respectively. The locations of the blueshifted outflow clump B0 and clump A, along the $p$–$v$ cut, are shown.

P.A. $\sim$ 132° (Figure 11), shows that the maximum velocity increases from near the source to the position of B0, similar to the Hubble wedges of the red outflow clumps. We speculate that B0 traces a region where an underlying protostellar wind is entraining molecular gas.

A recent study of the HH 46/47 jet shows that the proper motion on the plane of the sky of one of the most recent ejections (within $\sim$3″ of HH 47 IRS) is along a line with a P.A. of about 40° on the plane of the sky, while further away ($\sim$35″) from the source the jet motion has a P.A. closer to 55° (Hartigan et al. 2011). Thus, it is very unlikely that the ejection responsible for B0 is part of the flow responsible for the HH 46/47 jet, and the most likely candidate for powering the outflow that drives B0 is the binary companion in the HH 47 IRS binary system not responsible for the main HH 46/47 outflow. Weaker and smaller outflows from binary components have been observed in other sources (e.g., HH 111, Cernicharo & Reipurth 1996; BHR 71, Parise et al. 2006; L1448C Hirano et al. 2010; IRAM 04191+1522, Lee et al. 2005, Chen et al. 2012), and we believe that HH 46/47 shows another case of drastically different outflows arising from binaries in the same system. Current observations of this system do not have the required angular resolution to resolve which outflow is powered by each of the binary components in HH 47 IRS.

Figure 11 shows that there is a clump (which we name A) with very low red (and blue) outflow velocities at about 30″ northwest of HH 47 IRS on what would be the counter lobe of the outflow associated with B0. The distance from the source to A is slightly more than the distance to B0, and the position of A is coincident with the edge of the globule seen in our CO channel maps (Figure 3). It is not clear if clump A arises from the counter ejection of B0 or if it is just cloud emission. Further observations are needed to ascertain the nature of this clump.

## 5. SUMMARY AND CONCLUSIONS

We present the first interferometric map of the molecular (CO) outflow associated with the well-known HH 46/47 flow, powered by HH 47 IRS. With our high-velocity (0.08 km s$^{-1}$) and angular ($\sim$3″) resolution ALMA Cycle 0 observations we have investigated the kinematics and morphology of the molecular outflow. The 4.′2 long mosaic map of the CO(1–0) emission covers the length of the HH 46/47 outflow from HH 47A, in the northeast, to HH 47C, in the southwest, and provides the data to study both the blueshifted and redshifted molecular outflow lobes in detail. Our main conclusions are as follows.

The unprecedented sensitivity of our data enable us to detect outflow emission at much higher velocities than previous CO(1–0) studies of the source; up to outflow velocities of about $-30$ and 40 km s$^{-1}$ in the blue and red lobes, respectively. Even though the very high velocity ($|v_{\rm out}| > 20$ km s$^{-1}$) emission is constrained to about 15″ (or 7000 AU) from the source, detection of this outflow emission results in significantly higher values of the outflow kinetic energy and momentum, compared to results from existing single-dish CO(1–0) observations. If HH 46/47 is representative of molecular outflows from low-mass stars, our results imply that other similar molecular outflows may be much more energetic and carry more momentum than previously thought. The HH 46/47 flow is the first molecular outflow from a low-mass star to be mapped in the ALMA Cycle 0 phase and subsequent ALMA observations using more antennas will provide even more sensitive maps. From our results we expect that future outflow studies with ALMA will show that outflows can have much more impact on their surrounding cloud than previously thought.

The blue and red molecular outflow lobes show very distinct morphologies and kinematics. The blueshifted lobe only extends up to about 30″ (14,000 AU) northeast from HH 47 IRS. The compact size of the molecular outflow lobe is due to the fact that the outflow-powering protostar resides at the edge of its parent globule and the protostellar wind is only able to push and accelerate a limited amount of molecular material before it leaves the cloud. The blueshifted lobe shows a very clear parabolic structure in both the integrated intensity map and in the position–velocity diagram along the outflow axis. The morphology and velocity distribution are consistent with a model where the molecular outflow is formed by the entrainment of an underlying wide-angle protostellar wind. We argue that the coexistence of a wide-angle molecular outflow and an optical jet in the blue lobe of HH 46/47 is possible if the underlying protostellar wind has both a collimated (jet) and a wide-angle component. In the blue lobe, the wide-angle wind component dominates the gas entrainment because the jet bow shocks lie in a region with very low ambient density while the wide-angle component interacts with the environment very close to the source, where there is enough ambient (molecular) gas for the wide-angle wind to entrain and form the observed molecular outflow.

The redshifted lobe is about 2′ ($\sim$0.3 pc) in length, extending out to the southwest edge of the globule. Within approximately 40″ (18,000 AU) of the source the red lobe shows a wide-angle structure which is very different from the loop-like structure seen in IR images and the CO lobe structure at greater distances from the source. Our results also show that, beyond 40″ and along the axis of the red lobe, the HH 46/47 outflow has three clumps clearly detected in the integrated intensity map and position–velocity diagram. Their spatial distribution and velocity structure indicate that these clumps arise from prompt entrainment, most probably produced by bow shocks, arising from quasi-periodic episodes of increased mass ejection in HH 47 IRS. We argue that, similar to the blue lobe, the underlying protostellar wind has both a collimated and a wide-angle component and that close to the protostar the molecular outflow red lobe is dominantly driven by the wide-angle component

while the CO outflow observed beyond 40″ mainly arises from the entrainment by a collimated episodic wind. The wide-angle wind of this, or any other, outflow may affect the infall and the protostar's mass-assembling process, and future ALMA observations with higher angular resolution and using higher density tracers should concentrate on studying the impact of the wide-angle wind on the infalling core and circumstellar envelope.

The position of the three molecular outflow clumps along the axis of the redshifted lobe suggests that they are caused by the same ejection event that produced three major bow shocks in the blue lobe observed in the optical. Our results confirm previous studies that indicate that HH 47 IRS goes through episodes of increased mass outflow (and accretion) rates every few hundred years. Future (higher resolution) multi-epoch observations with ALMA may be able to detect the proper motion of the bow-shock-driven outflow clumps in HH 46/47 and other molecular outflows. These studies could help in our understanding of outflow variability and constrain variable accretion models.

Our high-velocity resolution data allowed us to study the kinematics of the outflow cavity and search for signatures of outflow rotation. We find, in both blue and red lobes, there is outflow emission over a wide range of velocities at the cavity walls, and the existence of a gradual gradient where the velocity increases toward the outflow axis. It is not clear what produces this velocity structure. Yet, we are certain it is not consistent with outflow rotation. Future comparison of our data with numerical models will allow us to investigate the origins of this kinematic behavior in the entrained gas.

Our CO(1–0) data detect a small clump at blueshifted velocities southeast of HH 47 IRS, which we believe arises from the interaction of a protostellar wind driven by the binary component in HH 47 IRS that does not drive the main HH 46/47 outflow. The clump, which lies at a P.A. very different from that of the main HH 46/47 flow, has a velocity distribution consistent with it being formed by bow-shock prompt entrainment. Future observations with an order of magnitude higher angular resolution than the maps presented here will be able to confirm our results and resolve which outflow is powered by each of the binary components in HH 47 IRS.

H.G.A. acknowledges support from his NSF CAREER award AST-0845619. D.M. and G.G. gratefully acknowledges support from CONICYT project BASAL PFB-06. We thank Chin-Fei Lee for his help with the wide-angle model. This paper makes use of the following ALMA data: ADS/JAO.ALMA#2011.0.00367.S. ALMA is a partnership of ESO (representing its member states), NSF (USA), and NINS (Japan), together with NRC (Canada) and NSC and ASIAA (Taiwan), in cooperation with the Republic of Chile. The Joint ALMA Observatory is operated by ESO, AUI/NRAO, and NAOJ. The National Radio Astronomy Observatory is a facility of the National Science Foundation operated under cooperative agreement by Associated Universities, Inc.

*Facility:* ALMA

## REFERENCES

Antoniucci, S., Nisini, B., Giannini, T., & Lorenzetti, D. 2008, A&A, 479, 503
Arce, H. G., & Goodman, A. A. 2001a, ApJL, 551, L171
Arce, H. G., & Goodman, A. A. 2001b, ApJ, 554, 132
Arce, H. G., & Goodman, A. A. 2002, ApJ, 575, 928
Arce, H. G., & Sargent, A. I. 2004, ApJ, 612, 342
Arce, H. G., & Sargent, A. I. 2006, ApJ, 646, 1070
Bachiller, R., Martin-Pintado, J., Tafalla, M., Cernicharo, J., & Lazareff, B. 1990, A&A, 231, 174
Bally, J., Reipurth, B., Lada, C. J., & Billawala, Y. 1999, AJ, 117, 410
Bence, S. J., Richer, J. S., & Padman, R. 1996, MNRAS, 279, 866
Bourke, T. L., Garay, G., Lehtinen, K. K., et al. 1997, ApJ, 476, 781
Cabrit, S., & Bertout, C. 1990, ApJ, 348, 530
Cabrit, S., & Raga, A. 2000, A&A, 354, 667
Cabrit, S., Raga, A., & Gueth, F. 1997, in IAU Symp. 182, Herbig-Haro Flows and the Birth of Stars, ed. B. Reipurth & C. Bertout (Dordrecht: Kluwer), 163
Cernicharo, J., & Reipurth, B. 1996, ApJL, 460, L57
Chen, X., Arce, H. G., Dunham, M. M., & Zhang, Q. 2012, ApJL, 747, L43
Chernin, L. M., & Masson, C. R. 1991, ApJL, 382, L93
Choi, M., Kang, M., & Tatematsu, K. 2011, ApJL, 728, L34
Dunham, M. M., Arce, H. G., Bourke, T. L., et al. 2012, ApJ, 755, 157
Eislöffel, J., Davis, C. J., Ray, T. P., & Mundt, R. 1994, ApJL, 422, L91
Eislöeffel, J., & Mundt, R. 1994, A&A, 284, 530
Fendt, C. 2009, ApJ, 692, 346
Ferreira, J., Dougados, C., & Cabrit, S. 2006, A&A, 453, 785
Garcia Lopez, R., Nisini, B., Eislöffel, J., et al. 2010, A&A, 511, A5
Goodman, A. A., & Arce, H. G. 2004, ApJ, 608, 831
Gueth, F., Guilloteau, S., & Bachiller, R. 1996, A&A, 307, 891
Hartigan, P., Frank, A., Foster, J. M., et al. 2011, ApJ, 736, 29
Hartigan, P., Heathcote, S., Morse, J. A., Reipurth, B., & Bally, J. 2005, AJ, 130, 2197
Hartigan, P., Morse, J. A., & Raymond, J. 1994, ApJ, 436, 125
Heathcote, S., Morse, J. A., Hartigan, P., et al. 1996, AJ, 112, 1141
Hirano, N., Ho, P. P. T., Liu, S.-Y., et al. 2010, ApJ, 717, 58
Launhardt, R., Pavlyuchenkov, Y., Gueth, F., et al. 2009, A&A, 494, 147
Lee, C.-F., Hirano, N., Palau, A., et al. 2009, ApJ, 699, 1584
Lee, C.-F., & Ho, P. T. P. 2005, ApJ, 624, 841
Lee, C.-F., Ho, P. T. P., & White, S. M. 2005, ApJ, 619, 948
Lee, C.-F., Mundy, L. G., Reipurth, B., Ostriker, E. C., & Stone, J. M. 2000, ApJ, 542, 925
Lee, C.-F., Stone, J. M., Ostriker, E. C., & Mundy, L. G. 2001, ApJ, 557, 429
Lefloch, B., Cernicharo, J., Reipurth, B., Pardo, J. R., & Neri, R. 2007, ApJ, 658, 498
Li, Z.-Y., & Shu, F. H. 1996, ApJ, 472, 211
Machida, M. N., & Hosokawa, T. 2013, MNRAS, 431, 1719
Machida, M. N., Inutsuka, S.-i., & Matsumoto, T. 2011, ApJ, 729, 42
Matzner, C. D., & McKee, C. F. 2000, ApJ, 545, 364
Micono, M., Davis, C. J., Ray, T. P., Eisloeffel, J., & Shetrone, M. D. 1998, ApJL, 494, L227
Morse, J. A., Hartigan, P., Heathcote, S., Raymond, J. C., & Cecil, G. 1994, ApJ, 425, 738
Myers, P. C. 2008, ApJ, 687, 340
Nagar, N. M., Vogel, S. N., Stone, J. M., & Ostriker, E. C. 1997, ApJL, 482, L195
Nakamura, F., & Li, Z.-Y. 2007, ApJ, 662, 395
Noriega-Crespo, A., Moro-Martín, A., Carey, S., et al. 2004, ApJS, 154, 402
Noriega-Crespo, A., & Raga, A. C. 2012, ApJ, 750, 101
Offner, S. S. R., Lee, E. J., Goodman, A. A., & Arce, H. 2011, ApJ, 743, 91
Ohashi, N., Hayashi, M., Ho, P. T. P., & Momose, M. 1997, ApJ, 475, 211
Olberg, M., Reipurth, B., & Booth, R. S. 1992, A&A, 259, 252
Ossenkopf, V., & Henning, T. 1994, A&A, 291, 943
Parise, B., Belloche, A., Leurini, S., et al. 2006, A&A, 454, L79
Pech, G., Zapata, L. A., Loinard, L., & Rodríguez, L. F. 2012, ApJ, 751, 78
Pudritz, R. E., Ouyed, R., Fendt, C., & Brandenburg, A. 2007, in Protostars and Planets V, ed. B. Reipurth, D. Jewitt, & K. Keil (Tucson, AZ: Univ. Arizona Press), 277
Pudritz, R. E., Rogers, C. S., & Ouyed, R. 2006, MNRAS, 365, 1131
Raga, A., & Cabrit, S. 1993, A&A, 278, 267
Raga, A. C., Binette, L., Canto, J., & Calvet, N. 1990, ApJ, 364, 601
Raga, A. C., Noriega-Crespo, A., González, R. F., & Velázquez, P. F. 2004, ApJS, 154, 346
Reipurth, B. 1989, in Proc. ESO Workshop on Low Mass Star Formation and Pre-Main Sequence Objects, ed. B. Reipurth (Garching: ESO), 247
Reipurth, B. 2000, AJ, 120, 3177
Reipurth, B., & Heathcote, S. 1991, A&A, 246, 511
Reipurth, B., Yu, K. C., Heathcote, S., Bally, J., & Rodríguez, L. F. 2000, AJ, 120, 1449
Richer, J. S., Shepherd, D. S., Cabrit, S., Bachiller, R., & Churchwell, E. 2000, in Protostars and Planets IV, ed. V. Mannings, A. P. Boss, & S. S. Russell (Tucson, AZ: Univ. Arizona Press), 867
Schnee, S., Enoch, M., Johnstone, D., et al. 2010, ApJ, 718, 306
Schwartz, R. D. 1977, ApJL, 212, L25

Shang, H., Allen, A., Li, Z.-Y., et al. 2006, ApJ, 649, 845
Shang, H., Li, Z.-Y., & Hirano, N. 2007, in Protostars and Planets V, ed. B. Reipurth, D. Jewitt, & K. Keil (Tucson, AZ: Univ. Arizona Press), 261
Shu, F. H., Ruden, S. P., Lada, C. J., & Lizano, S. 1991, ApJL, 370, L31
Smith, M. D., Suttner, G., & Yorke, H. W. 1997, A&A, 323, 223
Stanke, T., McCaughrean, M. J., & Zinnecker, H. 1999, A&A, 350, L43
Suttner, G., Smith, M. D., Yorke, H. W., & Zinnecker, H. 1997, A&A, 318, 595
Tafalla, M., & Myers, P. C. 1997, ApJ, 491, 653
Tomida, K., Tomisaka, K., Matsumoto, T., et al. 2013, ApJ, 763, 6
van Kempen, T. A., Kristensen, L. E., Herczeg, G. J., et al. 2010, A&A, 518, L121
van Kempen, T. A., van Dishoeck, E. F., Güsten, R., et al. 2009, A&A, 501, 633
Velusamy, T., & Langer, W. D. 1998, Natur, 392, 685
Velusamy, T., Langer, W. D., & Marsh, K. A. 2007, ApJL, 668, L159
Vorobyov, E. I., & Basu, S. 2005, ApJL, 633, L137
Wampfler, S. F., Herczeg, G. J., Bruderer, S., et al. 2010, A&A, 521, L36
Yu, K. C., Billawala, Y., & Bally, J. 1999, AJ, 118, 2940
Zapata, L. A., Schmid-Burgk, J., Muders, D., et al. 2010, A&A, 510, A2
Zhu, Z., Hartmann, L., Gammie, C. F., et al. 2010, ApJ, 713, 1134